

Phase-sensitive interferometry of decorrelated speckle patterns

Dierck Hillmann^{1,2,*,†}, Hendrik Spahr^{2,3,†}, Clara Pfäffle^{2,3}, Sazan Burhan²,
Lisa Kutzner^{2,3}, Felix Hilge^{2,3}, and Gereon Hüttmann^{2,3,4}

¹Thorlabs GmbH, Maria-Goeppert-Straße 9, 23562 Lübeck, Germany

²Institute of Biomedical Optics, University of Lübeck, Peter-Monnik-Weg 4, 23562 Lübeck, Germany

³Medical Laser Centre Lübeck GmbH, Peter-Monnik-Weg 4, 23562 Lübeck, Germany

⁴Airway Research Center North (ARCN), Member of the German Center for Lung Research (DZL), Germany

* dhillmann@thorlabs.com

†These authors contributed equally

Abstract

Phase-sensitive coherent imaging exploits changes in the phases of backscattered light to observe tiny alterations of scattering structures or variations of the refractive index. But moving scatterers or a fluctuating refractive index decorrelate the phases and speckle patterns in the images. It is generally believed that once the speckle pattern has changed, the phases are scrambled and any meaningful phase difference to the original pattern is removed. As a consequence, diffusion and tissue motion below the resolution handicap phase-sensitive imaging of biological specimen. Here, we show that, surprisingly, a phase comparison between decorrelated speckle patterns is still possible by utilizing a series of images acquired during decorrelation. The resulting evaluation scheme is mathematically equivalent to methods for astronomic imaging through the turbulent sky by speckle interferometry. We thus adopt the idea

of speckle interferometry to phase-sensitive imaging in biological tissues and demonstrate its efficacy for simulated data and for imaging of photoreceptor activity with phase-sensitive optical coherence tomography. The described methods can be applied to any imaging modality that uses phase values for interferometry.

1 Introduction

Phase sensitive, interferometric imaging measures small changes in the time-of-flight of a light wave by detecting changes of its phase. But in many applications, statistical optical properties of the scattering structure randomize the phase of the backscattered light, resulting in a speckle pattern with random intensity and phase [1]. As a consequence, we can only extract meaningful phase differences from images with identical or at least almost identical speckle patterns [2]. However, if the detected wave's speckle pattern changes over time, it inevitably impedes phase sensitive imaging [3, 4]. For example, holographic interferometry or electronic speckle pattern interferometry (ESPI) compare at least two states of backscattered light acquired at different times, and it can only be applied if the respective speckle patterns are still correlated [2–5].

Among the most important effects that decorrelate speckles with time, are random motions and changes of the optical path length on a scale below the resolution, e.g., by diffusion [6, 7]. These effects are impossible to prevent. But also bulk sample motion can cause the phase evaluation to compare different parts of the same speckle pattern. While in 3D imaging this effect of bulk motion can often be corrected by co-registration and suitable algorithms, in 2D sectional imaging we lack the data to correct this as the acquired slices of the specimen change if the specimen moves perpendicularly to the imaging plane.

We recently demonstrated imaging of the activity

of photoreceptors and neurons by phase-sensitive full-field swept-source optical coherence tomography (FF-SS-OCT) [8,9]. Although FF-SS-OCT successfully measured nanometer changes of neurons and receptors due to activation over a few seconds, we could neither increase the measurement time, nor determine tissue changes in single cross-sectional scans (B-scans). In both cases speckle patterns changed after a few seconds due to diffusion, bulk tissue motion, or tissue deformations and the phase information was lost.

In this paper, we reconstruct phase changes over times significantly longer than the decorrelation time of the corresponding speckle patterns. The idea is to calculate phase difference in a series of consecutive images over small time differences that still show sufficient correlation. If this is done for several measurements with different speckle patterns, averaging of these independent measurements will cancel the contributions of the disturbing phase. Integrating all these phase differences then yields the real time evolution of the phase. By averaging the phase in multiple speckles to obtain a single phase value, the real phase change can be obtained beyond the correlation time of the speckles. In essence, we combine the information from multiple speckles, each of which carries information on phase changes over a certain time (see Fig. 1a).

Just integrating the phase difference of successive frames followed by a summation, as it is commonly used for phase unwrapping [10–14], accumulates the phase noise; except for phase unwrapping it is mathematically equivalent to a direct phase comparison. Without averaging, calculating short time phase differences will not yield any information about phase differences of uncorrelated speckle patterns. The averaging of short time phase differences before integration is the essential step as it effectively cancels the phase noise.

In the 1970s and 1980s the same idea, known as speckle interferometry, was originally used in astronomy for successful imaging through the turbulent atmosphere with diffraction limited resolution [1, 15–22]. Short time exposures were used to reconstruct the missing phase of the Fourier transform of diffraction limited undisturbed images: By utilizing a large number of short-exposure images with different disturbances, true and undisturbed phase differences for small distances in the aperture plane could be computed. From these phase differences the complete phase was recon-

structed by integration. We will frame the similarities and the mathematical analogy between the two methods, which allows us to benefit from advances in astronomy for interferometric measurements during coherent imaging.

Methods that allow phase evaluation beyond the correlation time have also been developed for synthetic aperture radar (SAR) interferometry (InSAR) [23,24]. In InSAR, phase evaluation is used to monitor ground elevation, but small changes on the ground or turbulence in the sky interfere with an evaluation of the phase [23] similar to interferometric measurements in biological imaging. For InSAR, two techniques have been developed which selectively evaluate the phase from only minimally affected images or structures. The first technique is referred to as small baseline subset technique (SBAS, [25]). It selects optimal images from a time series to compare phase values based on good correlation. The other method only compares phases of single selected scatterers that maintain good correlation over long times, so called permanent scatterers [26].

In the first part of this paper, we lay down the basics and establish the commonality between coherent phase-sensitive imaging and astronomic speckle interferometry. Afterwards, we demonstrate the efficacy of the resulting methods by simulating simple phase resolved images in backscattering geometry and evaluating these with the proposed approach. Finally, we apply our method to in vivo data of phase-sensitive optical coherence tomography. In a future paper, we will concentrate on details of the algorithm, optimizing the time step for computing the phase differences, and showing its advantages in different applications.

2 Theory

2.1 Mathematical formulation of the problem

We assume coherent imaging of the physical system, in which a deterministic change of the optical path length, e.g., swelling or shrinking of cells, is superimposed by random changes. These may be caused by diffusion, fluctuations of the refractive index, or rapid uncorrelated micro motion. The complex amplitude in each pixel of a coherently acquired and focused image can be represented as a sum of (random) phasors (complex values), where each summand comprises amplitude and

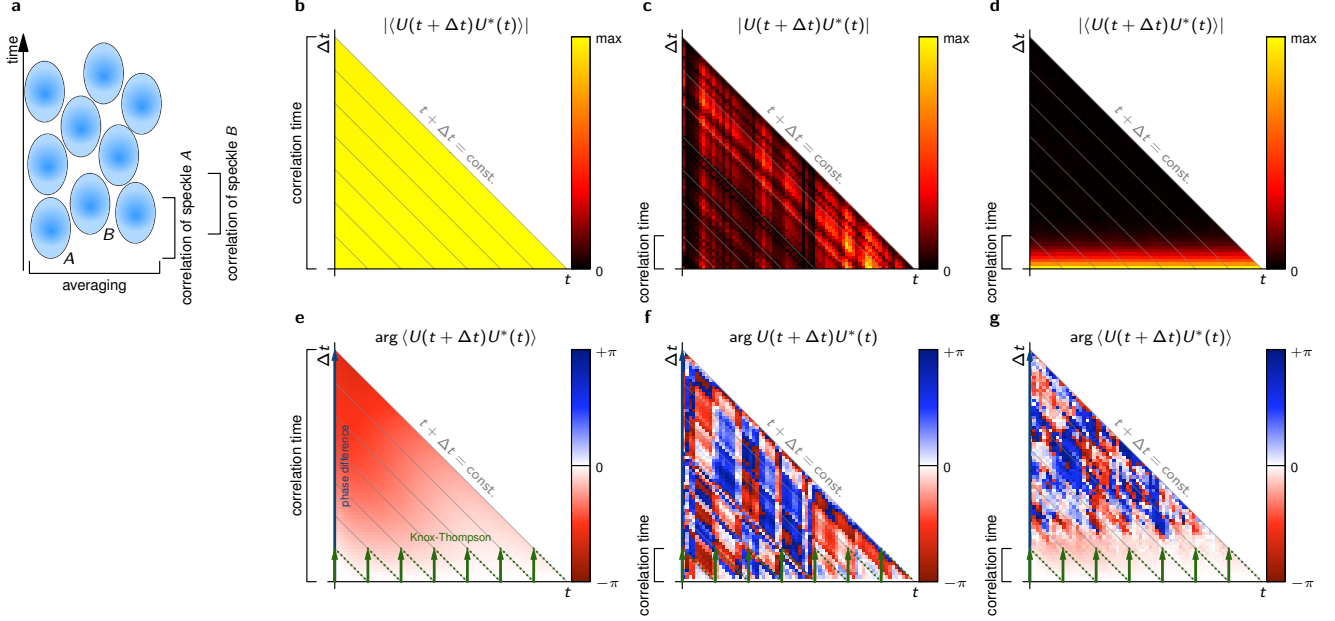


Figure 1: a) In average, each speckle (schematically represented by the blue ellipses) carries valid phase information only for its correlation time. Assuming that all speckle in the averaged area are subject to a common phase change in addition to random uncorrelated phase changes, one can use the phase of speckle *A* as long as it is valid and then continue with the phase of speckle *B*. Using multiple speckle, phase information for times significantly exceeding the correlation time can be extracted. b, e) Exemplary cross-spectrum magnitude and phase assuming infinite correlation time. Total phase changes can either be computed directly (blue arrow), or using the Knox-Thompson path (green arrows). c, f) Magnitude and phase of the cross-spectrum without averaging; neither method can extract the phase beyond the correlation time. d, g) Magnitude and phase of ensemble averaged cross-spectrum. Direct phase differences (blue) cannot be used for phase extraction, but Knox-Thompson (green) method can be applied since phase values for small Δt are valid.

phase. Such a coherently acquired field $U(\mathbf{x}, t)$ has contributions from the random phases $\phi_i(\mathbf{x}, t)$ and a systematic phase $\phi(\mathbf{x}, t)$. $U(\mathbf{x}, t)$ may then be written as

$$U(\mathbf{x}, t) = \sum_i A_i(\mathbf{x}, t) e^{i\phi_i(\mathbf{x}, t)} e^{i\phi(\mathbf{x}, t)}, \quad (1)$$

where A_i represents the unknown amplitude of each scatterer, and \mathbf{x} and t denote location and time, respectively. Depending on the imaging scenario, U might not depend on the location \mathbf{x} at all or \mathbf{x} might be up to three-dimensional as in tomographic imaging.

We can now separate U into its systematic phase contribution U_0 and a random modifier H , which yields

$$U(\mathbf{x}, t) = \underbrace{\left(\sum_i A_i(\mathbf{x}, t) e^{i\phi_i(\mathbf{x}, t)} \right)}_{H(\mathbf{x}, t)} \underbrace{e^{i\phi(\mathbf{x}, t)}}_{U_0(\mathbf{x}, t)} \quad (2)$$

$$= H(\mathbf{x}, t) U_0(\mathbf{x}, t).$$

The modifier H covers all effects that alter the speckle patterns over time, e.g., changing phase, changing amplitude, and scatterers moving out of or into the detection area. In this form, we have no way to distinguish H from U_0 . We can, however, compute the ensemble average by

$$\langle U(\mathbf{x}, t) \rangle = \langle H(\mathbf{x}, t) \rangle U_0(\mathbf{x}, t), \quad (3)$$

when assuming that U_0 (though not H) is constant over the averaged ensemble. The ensemble could consist of repeated measurements or certain pixels from a volume, in which U_0 is constant. In this averaged expression, we can now obtain the time evolution of U_0 for times where $\langle H \rangle$ remains approximately constant, i.e., where the contribution of the random phases is small. For t exceeding the correlation time of $\langle H \rangle$, however, the decorrelation of $\langle H \rangle$ still prevents us from computing changes in the systematic phase U_0 .

2.2 Solving the phase problem in astronomical speckle interferometry

The resolution of large ground-based telescopes is limited by atmospheric turbulences, which modify the phase of the optical transfer function (OTF) and cause time varying speckles in the image. During a long exposure these speckle patterns average out to a blurred image. Speckle interferometry is a way to obtain one diffraction limited image from several short exposure images. In each of these images the random atmospheric turbulences are constant and each image essentially contains one speckle pattern [1]. If the actual diffraction limited image of the object is $I_0(\mathbf{x})$ and has a Fourier spectrum $\tilde{I}_0(\mathbf{k})$, the Fourier spectra of the short exposure images are given by

$$\tilde{I}(\mathbf{k}) = \mathcal{H}_S(\mathbf{k})\tilde{I}_0(\mathbf{k}), \quad (4)$$

where \mathcal{H}_S is the short exposure OTF [1]. \mathcal{H}_S represents the disturbing effect of the atmosphere, changes randomly in each acquired image, and causes speckle noise in each image $I(\mathbf{x})$. A single short exposure image $I(\mathbf{x})$ will thus not yield the object information because phase and magnitude of \mathcal{H}_S are not known. However, the magnitude of the spectrum $\tilde{I}_0(\mathbf{k})$ of the diffraction limited images is obtained by averaging the squared magnitude of all short exposure spectra $\tilde{I}(\mathbf{k})$,

$$\left\langle \left| \tilde{I}(\mathbf{k}) \right|^2 \right\rangle = \left\langle \left| \mathcal{H}_S(\mathbf{k}) \right|^2 \right\rangle \left| \tilde{I}_0(\mathbf{k}) \right|^2, \quad (5)$$

since the squared short exposure OTF averaged over all measurements $\left\langle \left| \mathcal{H}_S(\mathbf{k}) \right|^2 \right\rangle$ is larger than zero and can be computed on the basis of known statistical properties of \mathcal{H}_S [1]. But the magnitude $\left| \tilde{I}_0 \right|$ of the Fourier spectrum only allows computation of the autocorrelation of I_0 . To obtain the full diffraction limited image the phase of $\tilde{I}_0(\mathbf{k})$ is required too. This phase is contained in the Fourier transforms $\tilde{I}(\mathbf{k})$ of the short time exposures, but it is corrupted by a random phase contribution of the atmospheric turbulences in the same way as the systematic phase in coherent imaging is corrupted by random phase noise.

Hence, retrieving diffraction limited images by speckle interferometry faces the same problem as retrieving the temporal phase evolution in coherent imaging. Only over small spatial frequency distances in the Fourier plane the phase difference in a spectrum $\tilde{I}(\mathbf{k})$ corresponds to the phase difference in the

spectrum $\tilde{I}_0(\mathbf{k})$ of the diffraction limited image. Over larger distances the phase information is lost due to atmospheric turbulence. The similarity of the problem is seen in the analogy of Equations (4) with (2), where \mathcal{H}_S and I correspond to H and U , respectively. However, while the astronomical problem has a two dimensional vector \mathbf{k} of spatial frequencies as dependent variable, the phase-sensitive imaging problem has only the time t . Both use a series of measurements, in which only phase information over small $\Delta\mathbf{k}$ or Δt is contained, respectively. We will show that by analyzing a large number of measurements, in which the corrupting phase contribution changes, the full phase can be reconstructed.

2.3 Phase information in the cross-spectrum

In astronomy, it were Knox and Thompson who solved the recovery of phases from statistical short exposure images [15] using the so-called cross-spectrum. Later, another approach, called the tripple-correlation or bispectrum technique, even improved the achieved results [16]. One major advantage of the bispectrum over the cross-spectrum technique for astronomical imaging is that it is only sensitive to the non-linear phase contributions to the transfer function \mathcal{H}_S , since shifted images yield to the same bispectrum and do not pollute the obtained phases (see, for example, [17] for details). However, for phase sensitive imaging, the linear part of the phase evolution of U_0 is generally of interest and thus the bispectrum technique is not applicable here.

Following we will apply the algorithm of Knox and Thompson to recover the phase beyond the speckle correlation time in coherent imaging. For convenience, we will retain the term cross-spectrum, even though in our scenario it is evaluated in time-domain as a function of t rather than in (spatial) frequency-domain as a function of \mathbf{k} .

We define the cross-spectrum C_H of the phase disturbing speckle modulation H by

$$C_H(\mathbf{x}, t, \Delta t) = H(\mathbf{x}, t)H^*(\mathbf{x}, t + \Delta t).$$

It is subject to speckle noise since H itself merely contains speckle (Fig. 1c and f); but its ensemble average

$$\langle C_H(\mathbf{x}, t, \Delta t) \rangle = \langle H(\mathbf{x}, t)H^*(\mathbf{x}, t + \Delta t) \rangle \quad (6)$$

has in general a magnitude larger than 0 and speckles of H are averaged out, at least for small Δt . Most importantly, it is to a good approximation real-valued, i.e., its phase is zero, as long as Δt is within the correlation time of H . This real-valuedness was previously shown for $\langle C_{\mathcal{H}_S} \rangle$ in astronomic imaging [1, 21]. For phase imaging, we show the real-valuedness of $\langle C_H \rangle$ for small Δt for which the autocorrelation is still strong in the Methods section. If Δt is larger than the correlation time, $H(\mathbf{x}, t)$ and $H^*(\mathbf{x}, t + \Delta t)$ become statistically independent, the phase of $\langle C_H \rangle$ gets scrambled and C_H follows speckle statistics.

Now, if we again assume that U_0 and thus C_{U_0} are constant over the ensemble, we compute the averaged cross-spectrum of the measurements of U to

$$\begin{aligned} \langle C_U(\mathbf{x}, t, \Delta t) \rangle &= \langle U(\mathbf{x}, t)U^*(\mathbf{x}, t + \Delta t) \rangle \\ &= \langle C_H(\mathbf{x}, t, \Delta t) \rangle C_{U_0}(\mathbf{x}, t, \Delta t). \end{aligned}$$

Knowing that $\langle C_H \rangle$ is real-valued for small Δt , the phases of $\langle C_U \rangle$ are determined only by the phases of C_{U_0} . If we find phases of U_0 that yield the phases of $\langle C_U \rangle$ for these small Δt , we obtain the systematic phase $\phi(\mathbf{x}, t)$ we are looking for as introduced in (1).

Note that $\langle C_U(\mathbf{x}, t, \Delta t) \rangle$ is related to the time-autocorrelation of U , except averaging being performed over the ensemble instead of the time t and thus being a function not only of Δt but also of t . Due to this relation the cross-spectrum maintains comparably large magnitudes for time differences Δt with large autocorrelation values. The magnitudes and phases of exemplary cross-spectra, in the decorrelation-free scenario and with strong decorrelation, with and without the ensemble averaging (obtained from simulations, see Results and Methods) is shown in Figs. 1b to g. The figures illustrate that $\langle C_U \rangle$ yields a deterministic increase of the phases for small Δt (Fig. 1g) as long as its magnitude (Fig. 1d, related to the autocorrelation) remains large, but only if the ensemble averaging is performed. It can further be seen, that the valid phase differences visible in Fig. 1g are small compared to the phases for large t in Fig. 1e since they represent merely phase difference for small Δt . Nevertheless, when reconstructing the phase of U_0 from the values of $\langle C_U \rangle$, we need to ensure that only values for (small) Δt with strong autocorrelation are taken into account. This condition coincides with the real-valuedness of $\langle C_H \rangle$.

Ensemble averaging needs multiple independent measurements, which cannot be performed easily in

a real experiment. However, averaging over multiple lateral pixels or averaging over multiple detection apertures can be done from a single experiment and approximates the ensemble average. In our case we either use an area over which we strive to obtain one mean phase-curve, or we use a Gaussian filter with a width determined as a compromise between spatial resolution and sufficient averaging statistics to obtain images of the phase evolution (see Methods).

2.3.1 Phase retrieval from the cross-spectrum

Having obtained the cross-spectrum $\langle C_U \rangle$, the systematic phase function U_0 needs to be extracted. We assume a given initial phase $\phi(\mathbf{x}, t = t_0)$ and evaluate methods to extract the systematic phase evolution $\phi(\mathbf{x}, t)$ from the cross-spectrum: An approach equivalent to computing phase differences directly is given by

$$\phi(\mathbf{x}, t_0 + t) = \phi(\mathbf{x}, t_0) + \arg \langle C_U(\mathbf{x}, t_0, t) \rangle, \quad (7)$$

for $t \geq t_0$ (blue arrows in Figs. 1b-g). However, it only yields phases within the correlation time. In astronomy, this approach never works, unless the image was not disturbed by turbulence in the first place. Instead, Knox and Thompson originally demonstrated diffraction limited imaging through the turbulent sky [15] by iteratively walking in small increments of Δt (e.g., one time step) through the cross-spectrum, i.e.,

$$\begin{aligned} \phi(\mathbf{x}, t_0 + n\Delta t) &= \phi(\mathbf{x}, t_0 + (n-1)\Delta t) \\ &+ \arg \langle C_U(\mathbf{x}, t_0 + (n-1)\Delta t, \Delta t) \rangle, \quad (8) \end{aligned}$$

for integer $n \geq 1$ with increasing iteration number n (green arrows in Figs. 1b-g). This method uses only phase values well within the correlation time. If $\langle C_U \rangle$ is valid for the single time steps Δt , i.e., $\langle C_H \rangle$ is real valued, the iterative formula will yield valid results, even for larger t . However, a single outlier at a time t_{err} , i.e., one false step, ruins all following values for $t \geq t_{\text{err}}$.

The influence of these single events can be reduced by taking multiple ways with different Δt for stepping through the cross-spectrum. In astronomy, this is known as the extended Knox-Thompson method [17, 22]. However, most of the algorithms for finding the optimal paths have been developed for use with respect to the bispectrum technique [18–20]; nevertheless, in general they can be easily transferred to

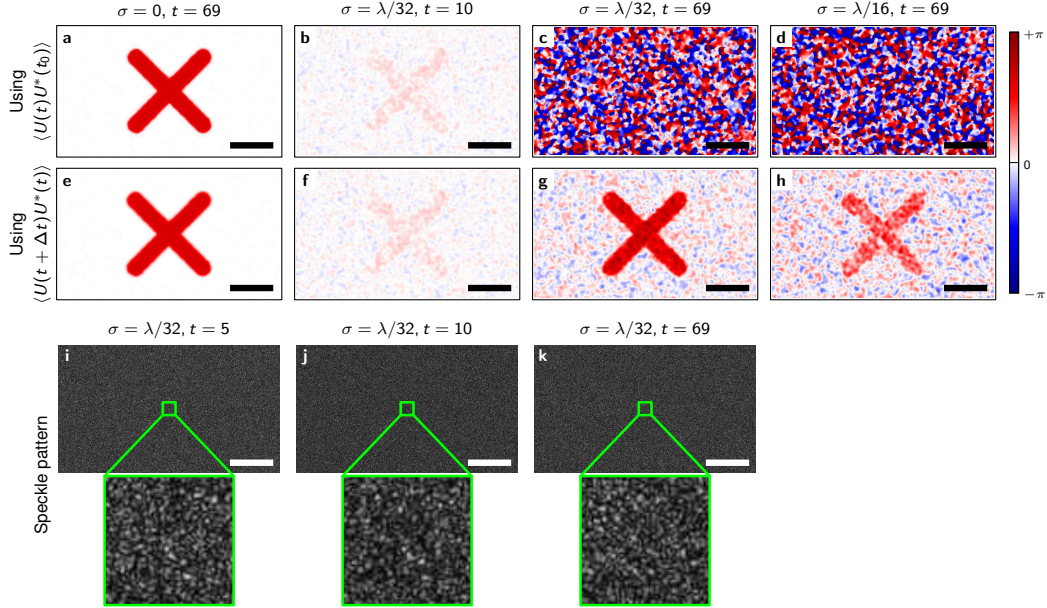


Figure 2: Phase images and speckle patterns obtained from the simulation. a-d) Phase evaluated by phase differences for different σ and time steps. e-h) Phase evaluated using the extended Knox-Thompson methods for the same σ and time steps as shown in (a)-(d). i-k) Speckle patterns for $\sigma = \lambda/32$ after a different number of time steps. Scale bars are 500λ .

the cross-spectrum. Here we minimized the sum of weighted squared differences between the measured cross-spectrum and the cross-spectrum resulting from the systematic phase $\phi(\mathbf{x}, t)$. The algorithm is described step-by-step in the methods section, and we will motivate, describe, and evaluate it in more depth in a future publication.

3 Results

3.1 Simulation

We simulated images of a large number of point scatterers that exhibit a random Gaussian-distributed 3-dimensional motion (with variance σ^2) in between frames in addition to a common axial motion in a specific “x”-shaped area. This simulation of degrading speckle clearly demonstrates the power of the extended Knox-Thompson method. For $\sigma = \lambda/32$, the phase evaluation with a simple phase difference to the first image and the extended Knox-Thompson method yield almost indistinguishable results for the first 10 steps (Fig. 2b and f). After 60 time steps, a simple phase difference to the first image yields only noise (Fig. 2c), while the “x”-shaped pattern is still well visible (Fig. 2g) using the extended Knox-Thompson method. The speckle

patterns appear correlated after 10 steps, but are completely changed after 69 steps (Figs. 2i-k). Doubling the scatterer motion to $\sigma = \lambda/16$, the “x”-shaped pattern begins to deteriorate after 69 steps even with the Knox-Thompson method. However, the “x” remains visible (Fig. 2h), whereas the phase difference again yields only phase noise (Fig. 2d).

The curves extracted in multiple simulations from the “x” confirm the results of the images and demonstrate the reproducibility of the method. Without random scatterer motion ($\sigma = 0$, Fig. 3a,e and Fig. 2a,e), the phase can be calculated by the phase difference to the first frame yielding the exact curve that was supplied to the simulation. But introducing random Gaussian-distributed motion of the scatterers with as little as $\sigma = \lambda/32$ between frames accumulates huge errors in the phase of the directed motion after 70 frames (Fig. 3b); the mean autocorrelation of the complex fields (Fig. 3i) in this case drops to one half in less than ten frames. Increasing motion amplitude (Fig. 3c and d) has devastating effects on the calculated phase differences. Retrieving the phase with the cross-spectrum based Knox-Thompson method yields the directed motion up to $\sigma = \lambda/16$ (Fig. 3f, g, and h) even though the autocorrelation halves after few frames (Fig. 3k).

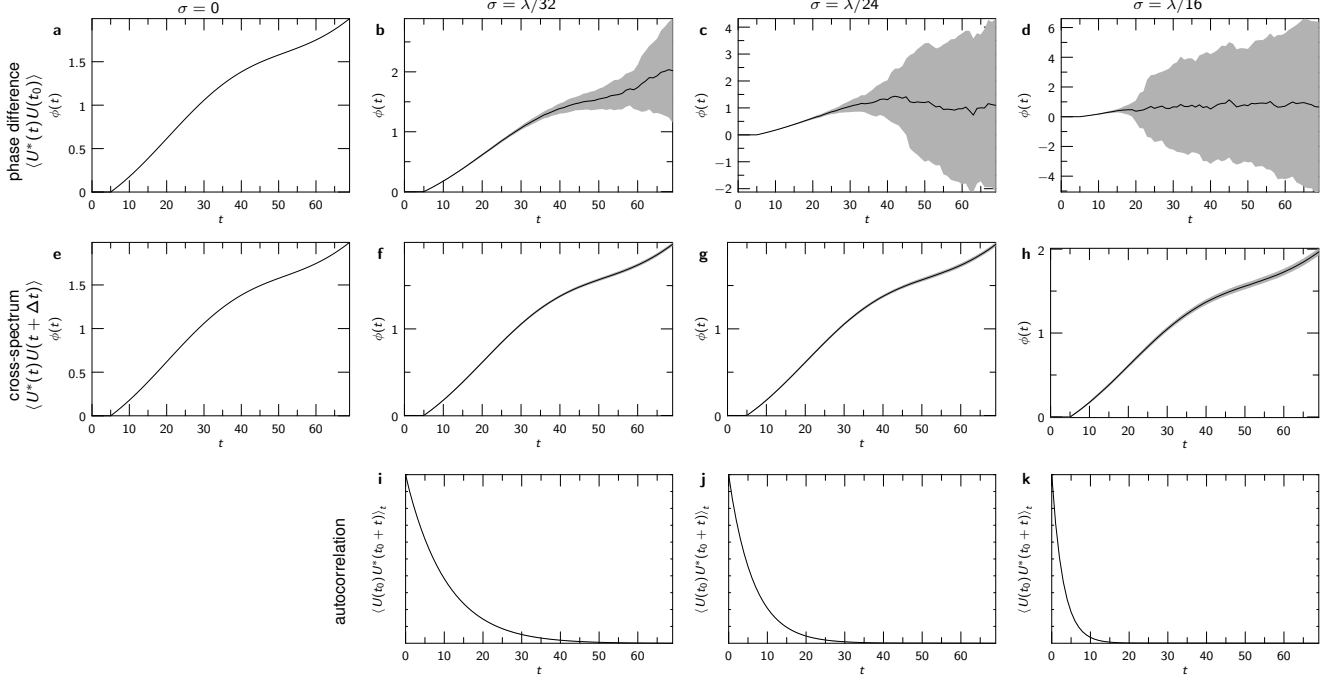


Figure 3: Extracting a single phase curve from simulated images of point scatterers that move between successive measurements by subtracting the phase of the first image (a-d) and Knox-Thompson evaluation of phases (e-h) while random 3D motion of the simulated scatterers is increased from 0 to $\lambda/16$. i-k) Autocorrelation of temporal changes of the wave field. The autocorrelation has been normalized to 1 for $t = 0$. Each curve was simulated $100\times$; the gray areas indicate the standard deviation of the obtained values.

3.2 In vivo experiments

The in vivo experiments confirm the simulation results. Here, we imaged human retina with full-field swept-source optical coherence tomography (FF-SS-OCT, Fig. 5), which provides three-dimensional tomographic data comprising amplitude and phase, to show the elongation of photoreceptor cells in the living human retina. Phase differences between both ends of the photoreceptor outer segments were evaluated after stimulating the photoreceptors with an “x”-shaped light-stimulus, similar to the simulation (see Methods). Figs. 4a-g show the extracted phase difference of the 5th frame (the beginning of the stimulus) to various other frames of the data set. The last frame was acquired 14.6 seconds later. After 5 seconds the phase differences are dominated by random phases and the speckle patterns of the compared images changed considerably after this time (Figs. 4o-u). Diffusion and uncorrected tissue motion are likely to be the dominant factors. The phase evaluation using the cross-spectrum is nevertheless able to reconstruct the phase difference and show the elongation of the photoreceptor outer segments

(Figs. 4h-o). Even in the non-stimulated area of Fig. 4g, it is clearly seen that the phase difference gives random results, whereas the extended Knox-Thompson approach shows the expected small changes (Fig. 4n).

4 Conclusion

Building the phase differences of successive frames, and then summing or integrating the differences has been used in phase sensitive imaging [10–14]. It removes the burden of phase unwrapping and thereby improves results. In contrast, including an average over multiple speckles after computing the phase differences and before integrating those differences again, as done by the Knox-Thompson method in astronomic speckle interferometry, allows phase sensitive imaging over more than ten times the speckle decorrelation time. To our knowledge, this important step has never been fully realized in phase sensitive imaging. The resulting method overcomes limitations from decorrelating speckle patterns and recovers phase differences even if speckle are completely decorrelated. Using extended Knox-Thompson

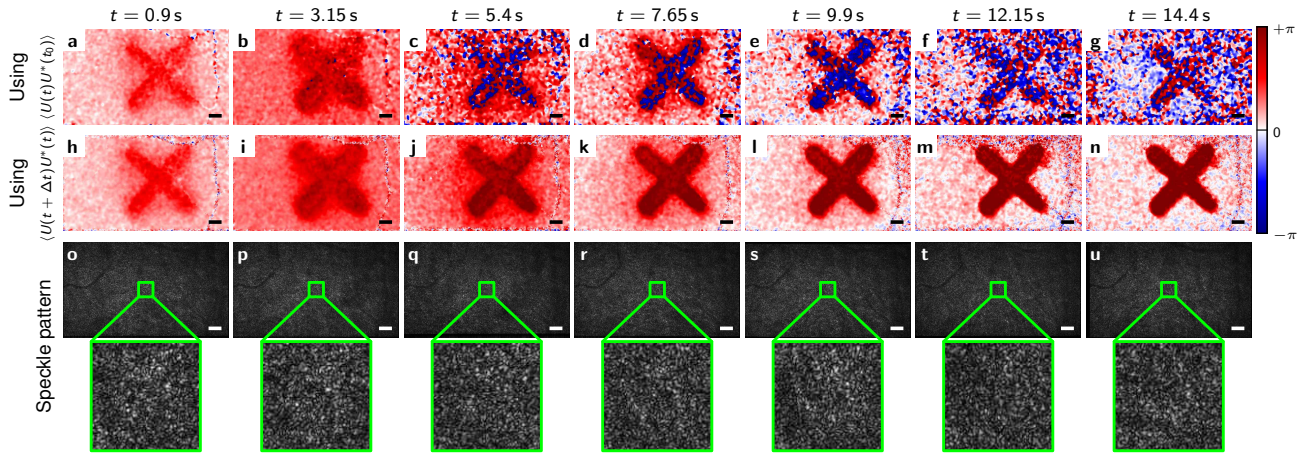


Figure 4: Phase differences between the ends of the photoreceptor outer segment in the living human eye at different times compared to the initial phase at $t = 0$. The entire measurement ended at about $t = 14.6$ s after initiating a light stimulus. a-g) Phase difference obtained by directly comparing to pre-stimulus phase with phase after different times. h-n) Phase difference obtained from the cross-spectrum as described in the Methods section (by minimizing (13)). o-u) Speckle pattern of one of the involved layers before the stimulus and at the respective times. It can clearly be seen, that that the speckle pattern changes with time. Scale bars are $200 \mu\text{m}$.

methods yields the optimized results presented here and removes the sensitivity to outliers.

Still, measurements and the algorithm can be further improved in several regards. We approximated the ensemble average either by averaging a certain area of lateral pixels or by a Gaussian filter. The former is suitable to obtain the mean expansion in a certain area, the latter is used to obtain images. But to get high-resolution images, using spatial filtering is not ideal. Other speckle averaging techniques, e.g., based on non-local means [27, 28], and time-encoded manipulation of the speckle pattern by deliberately manipulating the sample irradiation (similar to [29]) should preserve the full spatial resolution.

Increasing the sampling rate of the t axis of the cross-spectrum, i.e., decreasing the smallest Δt , should also improve results, since then the correlation of compared speckle patterns is improved. The results presented here are limited by the finite sampling interval of the t -axis and not by the overall measurement time; however, at some point it is expected that errors add up for high frequent sampling of t as data size increases further. Alternatively, one could acquire two immediate frames with a small Δt , followed by a larger time gap to the next two frames (during which speckle patterns can begin to decorrelate). The immediate frames can give the correct current rate of phase changes (the first derivative of the phase change) that can then be ex-

trapolated linearly to the time of the next two frames, etc. Obviously, this can be extended to three or more frames with small Δt giving the second or even higher order local derivative, respectively.

There are also extensions of the presented method possible. For example, the extraction of systematic phase changes in a dynamic, random speckle pattern can be combined with dynamic light scattering (DLS) [6, 7] basically separating the random diffusion from systematic particle motion. This approach might possibly give additional contrast compared to either method on its own.

Overall, applications of phase sensitive imaging over long times are manifold. Applications range from biological phase imaging to measure retinal pulse waves [14], detect cellular activity [8, 9], all the way to visualize deformations using electronic speckle interferometry.

References

- [1] Goodman, J. *Speckle Phenomena in Optics: Theory and Applications* (Roberts & Company, 2007).
- [2] Creath, K. Phase-shifting speckle interferometry. *Appl. Opt.* **24**, 3053–3058 (1985).

- [3] Joenathan, C., Haible, P. & Tiziani, H. J. Speckle interferometry with temporal phase evaluation: influence of decorrelation, speckle size, and non-linearity of the camera. *Appl. Opt.* **38**, 1169–1178 (1999).
- [4] Lehmann, M. Decorrelation-induced phase errors in phase-shifting speckleinterferometry. *Appl. Opt.* **36**, 3657–3667 (1997).
- [5] Jones, R. & Wykes, C. De-correlation effects in speckle-pattern interferometry. *Opt. Acta* **24**, 533–550 (1977).
- [6] Berne, B. & Pecora, R. *Dynamic Light Scattering: With Applications to Chemistry, Biology, and Physics*. Dover Books on Physics Series (Dover Publications, 2000).
- [7] Goldburg, W. I. Dynamic light scattering. *Am. J. Phys.* **67**, 1152–1160 (1999).
- [8] Hillmann, D. *et al.* In vivo optical imaging of physiological responses to photostimulation in human photoreceptors. *Proc. Natl. Acad. Sci. U.S.A.* **113**, 13138–13143 (2016).
- [9] Pfäffle, C. *et al.* Functional imaging of ganglion and receptor cells in living human retina by osmotic contrast. *ArXiv e-prints* (2018). 1809.02812.
- [10] van Brug, H. & Somers, P. A. A. M. Speckle decorrelation: Observed, explained, and tackled. In Jacquot, P. & Fournier, J.-M. (eds.) *Interferometry in Speckle Light*, 11–18 (Springer Berlin Heidelberg, Berlin, Heidelberg, 2000).
- [11] Wang, R. K., Kirkpatrick, S. & Hinds, M. Phase-sensitive optical coherence elastography for mapping tissue microstrains in real time. *Appl. Phys. Lett.* **90**, 164105 (2007).
- [12] Li, P. *et al.* Phase-sensitive optical coherence tomography characterization of pulse-induced trabecular meshwork displacement in *ex vivo* nonhuman primate eyes. *J. Biomed. Opt.* **17**, 17 – 17 – 11 (2012).
- [13] An, L., Chao, J., Johnstone, M. & Wang, R. K. Non-invasive imaging of pulsatile movements of the optic nerve head in normal human subjects using phase-sensitive spectral domain optical coherence tomography. *Opt. Lett.* **38**, 1512–1514 (2013).
- [14] Spahr, H. *et al.* Imaging pulse wave propagation in human retinal vessels using full-field swept-source optical coherence tomography. *Opt. Lett.* **40**, 4771–4774 (2015).
- [15] Knox, K. T. & Thompson, B. J. Recovery of images from atmospherically degraded short-exposure photographs. *Astrophys. J.* **193**, L45–L48 (1974).
- [16] Lohmann, A. W., Weigelt, G. & Wirnitzer, B. Speckle masking in astronomy: triple correlation theory and applications. *Appl. Opt.* **22**, 4028–4037 (1983).
- [17] Ayers, G. R., Northcott, M. J. & Dainty, J. C. Knox-thompson and triple-correlation imaging through atmospheric turbulence. *J. Opt. Soc. Am. A* **5**, 963–985 (1988).
- [18] Lannes, A. Backprojection mechanisms in phase-closure imaging. bispectral analysis of the phase-restoration process. *Exp. Astron.* **1**, 47–76 (1989).
- [19] Marron, J. C., Sanchez, P. P. & Sullivan, R. C. Unwrapping algorithm for least-squares phase recovery from the modulo 2π bispectrum phase. *J. Opt. Soc. Am. A* **7**, 14–20 (1990).
- [20] Haniff, C. A. Least-squares fourier phase estimation from the modulo 2π bispectrum phase. *J. Opt. Soc. Am. A* **8**, 134–140 (1991).
- [21] Roggemann, M., Welsh, B. & Hunt, B. *Imaging Through Turbulence*. Laser & Optical Science & Technology (Taylor & Francis, 1996).
- [22] Mikurda, K. & Der Lühe, O. V. High resolution solar speckle imaging with the extended knox-thompson algorithm. *Sol. Phys.* **235**, 31–53 (2006).
- [23] Bamler, R. & Just, D. Phase statistics and decorrelation in SAR interferograms. In *Geoscience and Remote Sensing Symposium, 1993. IGARSS '93. Better Understanding of Earth Environment., International*, 980–984 vol.3 (1993).
- [24] Zebker, H. A. & Villasenor, J. Decorrelation in interferometric radar echoes. *IEEE T. Geosci. Remote* **30**, 950–959 (1992).

- [25] Lanari, R. *et al.* An overview of the Small BAseline Subset algorithm: A DInSAR technique for surface deformation analysis. In Wolf, D. & Fernández, J. (eds.) *Deformation and Gravity Change: Indicators of Isostasy, Tectonics, Volcanism, and Climate Change*, 637–661 (Birkhäuser Basel, Basel, 2007).
- [26] Ferretti, A., Prati, C. & Rocca, F. Permanent scatterers in SAR interferometry. *IEEE T. Geosci. Remote* **39**, 8–20 (2001).
- [27] Deledalle, C., Denis, L. & Tupin, F. NL-InSAR: Nonlocal interferogram estimation. *IEEE T. Geosci. Remote* **49**, 1441–1452 (2011).
- [28] Lucas, A. *et al.* Insights into titan’s geology and hydrology based on enhanced image processing of cassini radar data. *J. Geophys. Res. – Planet.* **119**, 2149–2166 (2014).
- [29] Liba, O. *et al.* Speckle-modulating optical coherence tomography in living mice and humans. *Nat. Commun.* **8**, 15845 (2017).
- [30] Hillmann, D. *et al.* Aberration-free volumetric high-speed imaging of in vivo retina. *Sci. Rep.* **6**, 35209 (2016).

Competing interests DH is an employee of Thorlabs GmbH, which produces and sells OCT systems. DH and GH are listed as inventors on a related patent application.

Acknowledgements This work was funded by the German Research Foundation (DFG), Project Holo-OCT HU 629/6-1.

5 Materials and Methods

5.1 Simulation

For the simulation we created a complex valued image series with 640×368 pixels and a pixel spacing of 4λ , where λ is the simulated light wavelength. To obtain an image series we created a collection of $50 \times 640 \times 368 = 11,776,000$ point scatterers each getting a random x , y , and z coordinate, as well as an amplitude A . While the x and y coordinate was distributed entirely random in the image area, the z coordinate was restricted between 0 and 10λ and the amplitude was equally distributed between 0 and 1. To create an

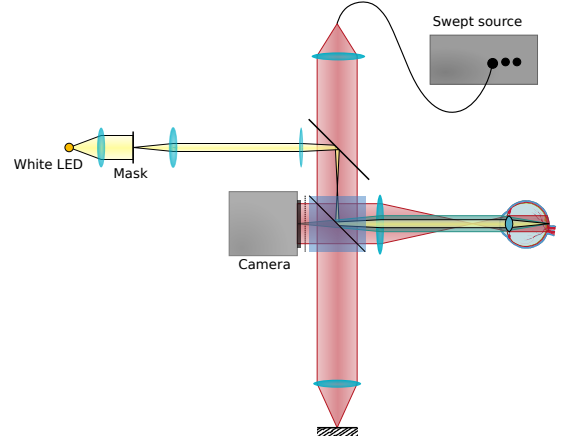


Figure 5: Full-field swept-source optical coherence tomography setup used for acquiring in vivo data.

image we iterated over all scatterers, and summed the values $A \exp(i2kz)$ for the pixel corresponding to the scatterer’s x and y coordinate, where z is the scatterer’s z -value, and $k = 2\pi/\lambda$. This basically corresponds to a phase one would obtain in reflection geometry when neglecting any possible defocus. Finally the image was laterally filtered simulating a limited numerical aperture (NA).

For each simulation we created a series of 70 images; starting with the initial scatterers, to create the next frame, we moved each scatterer randomly as specified by a Gaussian distribution with a certain variance σ^2 in x , y , and z direction. Furthermore, all scatterers currently having x and y -coordinates as found in a pre-created “x”-shaped mask were additionally subjected to the movement

$$\Delta z = \begin{cases} \frac{\lambda}{400} + \frac{\lambda}{800} \sin(0.1(t - t_0)) & t \geq t_0 \\ 0 & t < t_0 \end{cases},$$

where t is the frame number and $t_0 = 5$ in each frame.

5.2 Experiments

In vivo data was acquired with a Michelson interferometer-based full-field swept-source optical coherence tomography system (FF-SS-OCT) as shown in Fig. 5. The setup is similar to the system previously used for full-field and functional imaging [8, 14, 30]. Light from a Superlum BROADSWEEPER BS-840-1 is collimated and split into reference and sample arm. The reference arm light is reflected from a mirror and then directed by a beam splitter onto a high-speed area camera (Photron FASTCAM SA-Z). The sample light is directed in such a way, that it illuminates the retina with a collimated beam; the light backscattered by the retina is imaged through the illumination optics and the beamsplitter onto the camera, where it is superimposed with the reference light.

In addition the retina was stimulated with a white LED, where a conjugated plane to the retina contained an “x”-shaped mask. A low-pass optical filter in front of the camera ensured that the stimulation light does not reach the camera.

Swept laser, camera, and stimulation LED were synchronized by an Arduino Uno microprocessor board. It generates the trigger signals such that the laser sweeps $70\times$ for one dataset. During each sweep the camera acquires 512 images with 640×368 pixels each at a framerate of 60,000 frames/s. Each set of 512 images corresponds to one OCT volume. The stimulation LED is triggered after the first 5 volumes and remains active for the rest of the dataset. The time between volumes determines the overall measurement time. The number of 70 volumes was limited by the camera’s internal memory since the acquisition of the camera is too fast to stream the data to a computer in real time.

Measurement light had a centre wavelength of 841 nm and a bandwidth of 51 nm. About 5 mW of this light reached the retina illuminating an area of about $2.6\text{ mm}\times 1.5\text{ mm}$, which is the area imaged onto the camera. The “x”-pattern stimulation had significantly less irradiant power, of about $20\text{ }\mu\text{W}$ white light.

5.2.1 In vivo data acquisition

All investigations were done with healthy volunteers; written informed consent was obtained from all subjects. Compliance with the maximum permissible exposure (MPE) of the retina and all relevant safety rules was confirmed by the responsible safety officer. The study was approved by the ethics board of the University of Lübeck (ethics approval Ethik-Kommission Lübeck 16-080).

5.2.2 Data reconstruction

Data was reconstructed, registered and segmented as described in previous publications [9]: After a background removal the OCT signal was reconstructed by a fast Fourier transform (FFT) along the spectral axis. Next step was a dispersion correction by multiplication in the complex-valued volumes in the axial Fourier domain (after an FFT along the depth axis) with a correcting phase function that was determined iteratively by an optimization of sharpness metric of the OCT images [30]. Co-registering the volumes aligned the same structures in the same respective voxels of the data series. Finally, segmenting the average volume allowed aligning of the photoreceptor layers in a certain constant depth for easier phase extraction.

5.3 Phase evaluation

5.3.1 Computing the cross-spectrum

To compute the cross-spectrum, we took the series of OCT volumes $U(x, t)$ and computed the cross-spectrum by

$$C_U(x, t, \Delta t) = U(x, t)U^*(x, t + \Delta t).$$

5.3.2 Comparing phases of two different depths

For the in vivo experiments we additionally want to compare the phases between different ranges of layers. Let Z_1 and Z_2 denote the sets of layers, then we computed the effective phase difference cross-spectrum by

$$C_U^{Z_1-Z_2}(x, y; t, \Delta t) = \left(\sum_{z \in Z_1} C_U(x, y, z; t, \Delta t) \right) \times \left(\sum_{z \in Z_2} C_U(x, y, z; t, \Delta t) \right)^*, \quad (9)$$

where we now represented the vector \mathbf{x} by its components (x, y, z) . For the simulation, there is only one layer to be compared, and thus we set the phase difference cross-spectrum equal to the cross-spectrum of this one layer, i.e., $C_U^{Z_1-Z_2} = C_U$.

5.3.3 Approximating the ensemble average

To extract a curve the phase difference was approximated by averaging the cross-spectrum over the x and y coordinates belonging to a mask M , i.e.,

$$\langle C_U(t, \Delta t) \rangle_M \approx \frac{1}{|M|} \sum_{(x,y) \in M} C_U^{Z_1-Z_2}(x, y; t, \Delta t),$$

where $|M|$ is the number of pixels in the mask M .

To obtain images, instead, the ensemble average was approximated by applying a Gaussian filter (convolving with a Gaussian $G_{\sigma_{\text{Gauss}}^2}$ with variance σ_{Gauss}^2):

$$\langle C_U(x, y; t, \Delta t) \rangle \approx G_{\sigma_{\text{Gauss}}^2}(x, y) * C_U^{Z_1-Z_2}(x, y; t, \Delta t), \quad (10)$$

where $*$ is the convolution in x and y direction. In effect we used a circular convolution by using a fast Fourier transform (FFT) based algorithm.

5.3.4 The weights

We additionally used weights to specify how reliable the respective value of the cross-spectrum $\langle C_U \rangle$ is. Unfortunately, most algorithms that were used previously to compute weights in astronomy cannot be computed as efficiently

as $\langle C_U \rangle$, since we used a fast convolution to apply the Gaussian filter in equation (10). We therefore use the weights

$$w(t, \Delta t) = T \left(\sum_{(x,y) \in M} \frac{C_U^{Z_1-Z_2}(t, \Delta t)}{|C_U^{Z_1-Z_2}(t, \Delta t)|} - b \right) \quad (11)$$

for phase curve extraction and

$$w(x, y; t, \Delta t) = T \left(\left[G_{\sigma_{\text{Gauss}}}^2(x, y) * \frac{C_U^{Z_1-Z_2}(x, y; t, \Delta t)}{|C_U^{Z_1-Z_2}(x, y; t, \Delta t)|} \right] - b \right) \quad (12)$$

for phase imaging; both could be computed as efficiently as $\langle C_U \rangle$ itself. In these formula T is a cut-off function for negative values:

$$T(x) = \begin{cases} x & \text{for } x \geq 0 \\ 0 & \text{for } x < 0 \end{cases}$$

The truncation of negative values and the introduction of b are supposed to keep the expectation value for randomly distributed C_U at 0. The sum in (11) and the convolution term in (12) follow speckle statistics if the phase of C_U is random, since they are a sum of random phasors [1]. Consequently, a non-zero value is expected. This can be used to determine suitable values for b . The amplitude probability of a speckle pattern is given by a Rayleigh distribution [1]

$$p(A) = \frac{A}{\sigma^2} \exp\left(-\frac{A^2}{2\sigma^2}\right).$$

Enforcing a certain threshold A_0 gives a total probability

$$P_0(A_0) = \int_0^{A_0} dA' p(A') = 1 - e^{-\frac{A_0^2}{2\sigma^2}}$$

and its inverse

$$A_0(P_0) = \sqrt{-2\sigma^2 \ln(1 - P_0)}.$$

With this formula, we selected b to be the 99.999% threshold, i.e., $b = A_0(0.99999)$.

For the two scenarios of curve extraction and imaging with a Gaussian convolution, the parameter σ of the Rayleigh distribution remains to be determined. Starting with the derivation of speckle statistics [1], it can be computed to yield

$$\sigma = \frac{1}{\sqrt{2|M|}}$$

for curve extraction and

$$\sigma = \frac{1}{\sqrt{8\pi}\sigma_{\text{Gauss}}}$$

for imaging, when assuming unit magnitude phasors (as present in (11) and (12)) with completely random phases.

5.3.5 Phase unwrapping of the cross-spectrum

While alternate approaches to extract the phase from the cross-spectrum deal with the phase wrapping problem differently (e.g. [20]), for our scenario phases of the obtained cross-spectrum need to be unwrapped in the Δt axis in order to obtain good results. However, in 1D phase unwrapping, single outliers, i.e., a random phase for single specific Δt , can tremendously degrade results for all following values. We therefore slightly modified the standard 1D-phase unwrapping approach:

We assume the initial D phases to be free of wrapping. Afterwards we moved through the data set from small Δt to larger Δt . We computed the sum of all absolute values of the phase differences to the preceding D phases for each phase value that is to be determined. We increased or decreased the respective phase value by 2π as long as this difference sum kept decreasing. Then we move to the next Δt . This procedure was done once for curve extraction and repeated for each x and y value for imaging. In our scenario, we used $D = 10$.

5.3.6 Obtaining the phase from the cross spectrum

Instead of using the approaches described by (7) or (8), we formulate the recovery of the phases from the cross-spectrum as a linear least squares problem. This also served as basis for many of the previously demonstrated approaches in astronomy. Assuming the phase of the cross-spectrum is unwrapped in its Δt axis, we can assume that

$$\sum_{t, \Delta t} w^2(\mathbf{x}; t, \Delta t) \times |\phi(\mathbf{x}, t + \Delta t) - \phi(\mathbf{x}, t) - \langle C_U(\mathbf{x}; t, \Delta t) \rangle|^2 \quad (13)$$

minimizes for the desired phase $\phi(\mathbf{x}, t)$, if the weights w represent the quality of the cross-spectrum for the respective parameters \mathbf{x} , t , and Δt . However, the solution to this linear least square problem is not unique: since the cross-spectrum only contains phase differences, there will be different solutions for different initial values $\phi(\mathbf{x}, t = 0)$. In addition, all weights might be 0 for one specific t which represents a gap in reliable data. Both problems in the evaluation can be encountered by Tikhonov regularization with small parameters. For the former case one should force the resulting phase for one time point t_0 to be small; the corresponding regularization parameter should not influence other results as long as it is chosen sufficiently small to not introduce numerical errors. For the second problem, a difference regularization can be introduced. Again, the parameter can be small; it is only used is to obtain a unique solutions, in case weights approach 0. Consequently, the entire approach can

be formulated as a linear least squares problem, and solved by regularized solving of the respective linear equation.

To solve the least squares problem (13) we first need to discretize it properly. To this end, we first create the discrete vectors and matrices \mathbf{c}_ϕ corresponding to the unwrapped cross-spectrum phase $\arg(\langle C_U \rangle)$, ϕ corresponding to the phases to be extracted, and a matrix S relating the two. Assume a given systematic phase ϕ' , then the corresponding cross-spectrum \mathbf{c}'_ϕ would be uniquely given by

$$\mathbf{c}'_\phi = \begin{pmatrix} \phi'_0 - \phi'_1 \\ \phi'_0 - \phi'_2 \\ \vdots \\ \phi'_1 - \phi'_2 \\ \vdots \end{pmatrix} = \underbrace{\begin{pmatrix} 1 & -1 & 0 & \cdots & 0 \\ 1 & 0 & -1 & \cdots & 0 \\ & & \vdots & \ddots & \\ 0 & 1 & -1 & \cdots & 0 \\ & & \vdots & & \end{pmatrix}}_S \begin{pmatrix} \phi'_0 \\ \phi'_1 \\ \vdots \\ \phi'_{N-1} \end{pmatrix}.$$

We can write this as

$$\mathbf{c}'_\phi = S\phi'.$$

Given the actually measured cross-spectrum \mathbf{c}_ϕ and the corresponding phase ϕ to be computed and introducing the diagonal weight matrix $W = \text{diag}(w_0, w_1, \dots, w_{N-1})$ as computed by (11) or (12) we can write the determination of ϕ as the regularized minimization problem by

$$\|W(S\phi - \mathbf{c}_\phi)\|^2 + \mu_1 \|\Gamma_1 \phi\|^2 + \mu_2 \|\Gamma_2 \phi\|^2 \rightarrow \min.$$

The corresponding ϕ is found by

$$\phi = (S^T W^2 S + \mu_1^2 \Gamma_1^T \Gamma_1 + \mu_2^2 \Gamma_2^T \Gamma_2)^{-1} S^T W^2 \mathbf{c}_\phi,$$

which needs to be performed for each curve or each lateral pixel (x, y) when doing phase imaging. In general, we chose

$$\Gamma_{1,ij} = \begin{cases} 1 & \text{for } i = j = 4 \\ 0 & \text{otherwise} \end{cases}$$

and

$$\Gamma_{2,ij} = \begin{cases} 1 & \text{if } i = j \neq 0 \\ -1 & \text{if } i = j + 1 \\ 0 & \text{otherwise,} \end{cases}$$

with $\mu_1 = 0.02$ and $\mu_2 = 0.001$.

5.3.7 Specifying the initial value

The regularization term $\mu_1 \|\Gamma_1\|^2$ basically enforces the phase value corresponding to the 5th volume to 0, thereby specifying the initial value. Since in both, simulation and experiment, we only know that no (deliberate) phase change is occurring in the frames < 5 , we can normalize the final result by

$$\phi_{\text{res},i} = \phi_i - \frac{1}{N_0} \sum_{j=0}^{N_0-1} \phi_j,$$

with $N_0 = 5$.

5.3.8 Real-valuedness of the modulating cross-spectrum

For the entire approach to work it remains to be shown, that the modulation cross spectrum $\langle C_H \rangle$ is real-valued for small Δt . We assume the modulation cross-spectrum is given according to (2) and (6) by

$$\begin{aligned} \langle C_H \rangle &= \langle H(t)H^*(t + \Delta t) \rangle \\ &= \left\langle \left(\sum_i A_i(t)e^{i\phi_i(t)} \right) \left(\sum_j A_j(t + \Delta t)e^{i\phi_j(t + \Delta t)} \right)^* \right\rangle \\ &= \left\langle \sum_i A_i(t)A_i^*(t + \Delta t)e^{i(\phi_i(t) - \phi_i(t + \Delta t))} \right. \\ &\quad \left. + \sum_{i,j,i \neq j} A_i(t)A_j^*(t + \Delta t)e^{i(\phi_i(t) - \phi_j(t + \Delta t))} \right\rangle \\ &= \left\langle \sum_i A_i(t)A_i^*(t + \Delta t)e^{i(\phi_i(t) - \phi_i(t + \Delta t))} \right\rangle \\ &\quad + \left\langle \sum_{i,j,i \neq j} A_i(t)A_j^*(t + \Delta t)e^{i(\phi_i(t) - \phi_j(t + \Delta t))} \right\rangle. \end{aligned}$$

Now, the second term is small compared to the first term since ϕ_i and ϕ_j are statistically independent making the sum and the average run over random phasors. The phases of the first term can be approximated by $\phi_i(t) - \phi_i(t) + \partial_{t'} \phi_i(t')|_{t'=t} \Delta t = \partial_{t'} \phi_i(t')|_{t'=t} \Delta t$ and thus will be 0 for small Δt that are within good autocorrelation of the modulating function H . Thus $\langle C_H \rangle$ is real for small Δt to a good approximation.

5.4 Phase evaluation by phase differences

In the alternative approach we compute merely phase differences. We can still formulate this by using the cross-spectrum of phase difference $C_U^{Z_1 - Z_2}$ given by (9). For all values $t \geq t_0$, the phase is obtained by

$$\phi(t) = \arg \left\{ G_{\text{Gauss}} * C_U^{Z_1 - Z_2}(x, y; t_0, t) \right\}$$

for imaging and

$$\phi(t) = \arg \sum_{(x,y) \in M} C_U^{Z_1 - Z_2}(x, y; t_0, t)$$

for curve evaluation. For this direct phase computation, the phase-wrapped cross-spectrum was used. For curve extraction the phase was unwrapped in t afterwards.